

Article

Geochemical Behavior of Shallow Buried Nodules from Clarion–Clipperton Fracture Zone in the East Pacific: A LA-ICP-MS Mapping Analysis Perspective

Zedong Fan ^{1,2}, Xiaohu Li ^{1,2,3,*}, Zhenggang Li ^{1,2} , Weilin Ma ^{1,2}, Zhimin Zhu ^{1,2}, Jie Li ^{1,2}, Hao Wang ^{1,2}, Kehong Yang ^{1,2}, Huaiming Li ^{1,2} , Fengyou Chu ^{1,2} and Yanhui Dong ^{1,2,*} 

- ¹ Key Laboratory of Submarine Geosciences, Ministry of Natural Resources, Hangzhou 310012, China; fanzd@sio.org.cn (Z.F.)
² Second Institute of Oceanography, Ministry of Natural Resources, Hangzhou 310012, China
³ School of Oceanography, Shanghai Jiao Tong University, Shanghai 200030, China
* Correspondence: xhli@sio.org.cn (X.L.); dongyh@sio.org.cn (Y.D.)

Abstract: The Clarion–Clipperton Fracture Zone of the east Pacific contains numerous shallow buried nodules that are in direct contact with pore water in sediment, providing a direct reflection of the interaction between nodules and sediment. However, research on the geochemical behavior of these shallow-buried nodules is limited. This study used laser ablation inductively coupled plasma mass spectrometry (LA-ICP-MS), high-resolution transmission electron microscopy (HRTEM), and X-ray diffraction (XRD) to compare mineral and element distribution in shallow buried nodules with surface nodules. The shallow buried nodules are products of nodules entering the burial stage. In comparison to surface nodules, shallowly buried nodules develop a fourth oxidized-suboxic diagenetic growth layer after entering the burial stage, in addition to the three main growth inner layers (L1, L2, L3). We suggest that L4 is not influenced by the bottom water source and that the presence of todorokite and the high flux of Mn²⁺ in the sediment pore water compete with other metal elements to enter the lattice of manganate, resulting in significantly higher Mn, W, and Li contents in L4 compared to L2. However, the content of Ni, Mg, and other hydrogenetic elements is much lower in L4 compared to L2. We suggest that the instantaneous change in surface primary productivity results in a sudden shift in the redox environment of the upper sediment layer. This reaction leads to the reduction of solid-phase Mn, providing growth opportunities for the buried nodules. Simultaneously, this may also be the reason why the growth layer of the nodules is jointly controlled by the sedimentary processes of hydrogenetic, oxic diagenetic, and suboxic diagenetic processes.

Keywords: buried nodules; Clarion–Clipperton Fracture Zone; oxic-diagenetic; todorokite



Citation: Fan, Z.; Li, X.; Li, Z.; Ma, W.; Zhu, Z.; Li, J.; Wang, H.; Yang, K.; Li, H.; Chu, F.; et al. Geochemical Behavior of Shallow Buried Nodules from Clarion–Clipperton Fracture Zone in the East Pacific: A LA-ICP-MS Mapping Analysis Perspective. *Minerals* **2024**, *14*, 80. <https://doi.org/10.3390/min14010080>

Academic Editor: Hermann Kudrass

Received: 30 November 2023

Revised: 30 December 2023

Accepted: 5 January 2024

Published: 11 January 2024



Copyright: © 2024 by the authors. Licensee MDPI, Basel, Switzerland. This article is an open access article distributed under the terms and conditions of the Creative Commons Attribution (CC BY) license (<https://creativecommons.org/licenses/by/4.0/>).

1. Introduction

Deep-sea polymetallic nodules are abundant marine manganese deposits in the ocean that can absorb valuable rare and critical metals elements, making them economically valuable and commercially promising [1,2].

Manganese oxides, the primary constituent of deep-sea polymetallic nodules, play a crucial role in enriching various elements within the nodules [3,4]. These oxides selectively adsorb metal ions from bottom and pore water, forming growth layers through hydrogenetic and diagenetic processes [5,6].

Apart from surface manganese nodules, manganese nodules are widely found in seabed sediments, and they have been discovered in the Penrhyn Basin (PB), Central India Basin (CIB), and Clarion–Clipperton Fracture Zone (CCFZ). These buried nodules are in direct contact with pore water in sediment, providing a direct reflection of the interaction between nodules and sediment. However, research on the geochemical characteristics and formation processes of buried nodules is relatively limited [7,8].

Existing studies have indicated that buried nodules can have three potential fates: they can either continue to grow, dissolve, or remain unchanged [8], which is influenced by the position of the oxic-suboxic front (OSF) and burial depth within the sediment [9].

When the OSF is located at a deeper level within the sediment, Mn^{2+} ions are unable to migrate to the sediment surface and contribute to nodule growth [9,10]. In such cases, shallow buried nodules may stop growing [8]. Conversely, when the OSF is situated at a shallower depth, Mn^{2+} ions in the sediment pore water can be directly supplied to shallow buried nodules, allowing them to potentially continue growing. As the burial depth increases, the oxidation-reduction environment within the sediment promotes the reduction of manganese and iron oxides present in the nodules, resulting in the release of free ions into the pore water of the sediment [6,11]. This phenomenon contributes to the dissolution of nodules [12]. Consequently, dissolved nodules can appear as a result of this process.

The interaction between buried nodules and sediment pore water is a critical aspect to consider when studying the geochemical behavior of manganese oxides in sediments. In this study, GIS software (Arcmap 10.8) was used to extract elemental datasets from individual growth layers based on LA-ICP-MS scanning data. We compared the geochemical characteristics of typical surface and shallowly buried nodules in the western region of the CCFZ to elucidate the growth mode and element enrichment mechanism of polymetallic nodules after burial.

2. Geological Background of the Study Area

The sample collection area for this study (Figure 1) is located between the Clarion Clipperton Fracture Zone in the eastern Pacific Ocean. The structural characteristics of the CCFZ mainly include the Clarion and Clipperton fault zones, as well as parallel secondary or smaller transform faults, closely related to the history of plate evolution and activity in the Pacific region, formed by the late Mesozoic to Cenozoic seafloor expansion. The average depth of CCFZ is 5000 m, and the surface area has a large undulating terrain, with plains, sea hills, seamounts, depressions, ditches, and troughs arranged alternately.

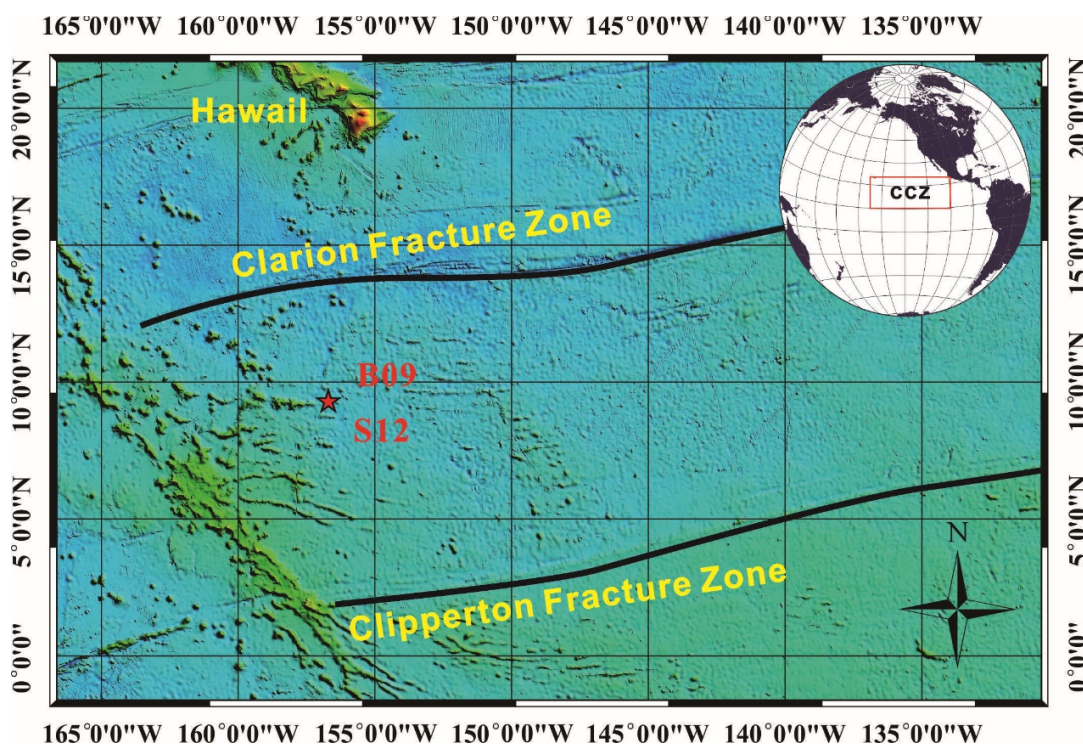


Figure 1. Locations of polymetallic nodules in this study. The red pentagrams represent the sample locations in this study (CCZ represents the Clarion–Clipperton Fracture Zone).

The study area specifically focuses on the western region of the CCFZ, where the basement formation dates to the Late Cretaceous period, approximately 95–65 million years ago. Gravity anomalies in this area reveal a low positive gravity background, indicating high-density mantle anomalies and seafloor uplift. Strong volcanic activity, well-developed faults, and the formation of large-scale volcanic chains and intermountain basin structures are prominent features of the study area.

The CCFZ is situated within an intermediate block of the Pacific Plate, located in a highly biologically productive area north of the equator. The primary productivity rate in the northeastern Pacific Ocean ranges between 0.1 and 0.2 kg C m⁻² yr⁻¹ [13,14]. It is noteworthy that surface primary productivity gradually decreases from east to west [15].

3. Materials and Methods

We selected typical co-existing surface nodules (S12) and buried nodules (B09, burial depth of approximately 60 cm) in the western part of CCFZ to ensure the representative nature of the results. Samples B09 and S12 (156.71° W, 9.33° N, collection depth: 5246 m) were all obtained through a box corer during the cruise DY73. The depth of nodule collection is deeper than the carbonate compensation depth (CCD: ~4500 m), and the sediment type in the collection area is pelagic clay.

Nodules were embedded in epoxy resin and sliced along the long axis direction from top to bottom. Each sample is further divided into two parts. Take half of each nodule and grind to 200 mesh using an agate mortar. The mineral composition of each nodule was analyzed by HRTEM and XRD. Concurrently, the other half was polarized and bonded to a glass slide, sectioned at a thickness of 100 µm for EPMA and LA-ICP-MS analyses.

3.1. X-ray Diffraction (XRD)

The X-ray diffraction analysis was performed using an X'Pert PRO X Advance diffractometer at the Instrument And Service Center for Physical Sciences of West Lake University in Hangzhou, China. The powdered samples were divided into three portions, with one portion measured directly, and the other two portions heated at 100 °C and 300 °C, respectively, for 24 h before XRD data collection. XRD was performed at 40 kV and 45 mA using a CuKα radiation source. The scanning angle ranges from 5° to 70° at a speed of 1.8°/min. The diffraction data were identified using MDI JADE software (version 6). For specific analysis and testing methods, please refer to [16].

3.2. High-Resolution Transmission Electron Microscopy (HRTEM)

Powders of nodules were further analyzed by HRTEM at the Guangzhou Institute of Geochemistry, Chinese Academy of Sciences. The analysis was conducted using an FEI Talos F200S field-emission transmission electron microscope equipped with two SuperX high-resolution energy-dispersive X-ray spectrometer (EDS) detectors and one high-angle annular dark-field (HAADF) detector. The analysis was performed at 200 kV voltage and included HRTEM and scanning transmission electron microscopy (STEM-EDS) analysis. The spatial resolution of the STEM mode is approximately 0.16 nm. Z-contrast images were acquired using a camera length of 160 mm to maximize the contrast changes between different atoms in HAADF images [17].

3.3. Laser Ablation Inductively Coupled Plasma Mass Spectrometry (LA-ICP-MS)

The trace elements surface scanning analysis was determined in Guangzhou Tuoyan Testing Technology Co., Ltd. This analysis involved the use of the NWR 193 nm ArF excimer laser ablation system, in conjunction with the iCAP RQ ICPMS. The ICP-MS was calibrated using NIST 610 and NIST 612 standard glasses [18] to ensure a low oxide production rate. During the testing process, the laser spot size was set to 100 µm, and the scanning speed was 120 µm/s. The energy density was set at 3.5 j/cm² with a repetition frequency of 15 Hz. The obtained data were processed using the Iolite software (version 4.0), and specific

analysis methods can be found in [16]. The data generated using Iolite were then gridded using ArcMap software (version 10.8).

For spot LA, a 50 μm spot size was used with an energy density of 5 J/cm^2 and a repetition frequency of 5 Hz. Each round of analysis comprised 20 s of background measurement (laser-off) and 45 s of data acquisition. Data calculations were performed using ICPMS DataCal, following the methods of [19,20].

3.4. Electron Microprobe Analyses (EMPA)

The major elements in the growth layer of B09 were analyzed in situ using the JEOL (Japan Electron) JXA-iSP100 electron probe microanalyzer at the Second Institute of Oceanography, Ministry of Natural Resources, China. The analysis was carried out with an accelerating voltage of 15 kV, a beam current of 10 nA, and a beam spot size of 10 μm . The ZAF method was used to perform baseline correction on all data. The UK MAC mineral/metal standards and the Chinese national standard sample GSB were utilized for calibration purposes. Specific regions of interest were selected within relatively homogeneous areas of the growth layer of B09 for the electron probe analysis.

4. Results

4.1. Structure Characteristics of Individual Growth Layer

The growth stages of nodules are divided based on the mineral reflectance and growth structure of the nodules.

The B09 nodule is divided into four individual layers (Figure 2a), with its core being an opal replaced by ferromanganese (Figure 2d). The L1 (~15 mm) is similar to the L3 (~5 mm), both of which have stromatolite structure, exhibiting alternating stacking of high reflectivity minerals and low reflectivity minerals at the micrometer scale, with good homogeneity and low porosity. L2 (~4 mm) has a laminated structure, with higher mineral reflectance than L1, poor homogeneity, loose layer structure, and extremely high porosity. Outside the L3, there is a thin (~0.3 mm) and dense like layer with high mineral reflectance and good uniformity, defined as the L4 (Figure 2b).

S12 is divided into three growth layers, among which L1 (10–20 mm) and L3 (4–10 mm) both have concentric circular structures with good homogeneity, low porosity, and overall low mineral reflectance. There is a high reflectivity mineral filling effect between the concentric circular structures. On the contrary, the L2 (2–10 mm) has a laminated structure with poor homogeneity, high porosity, and high mineral reflectance.

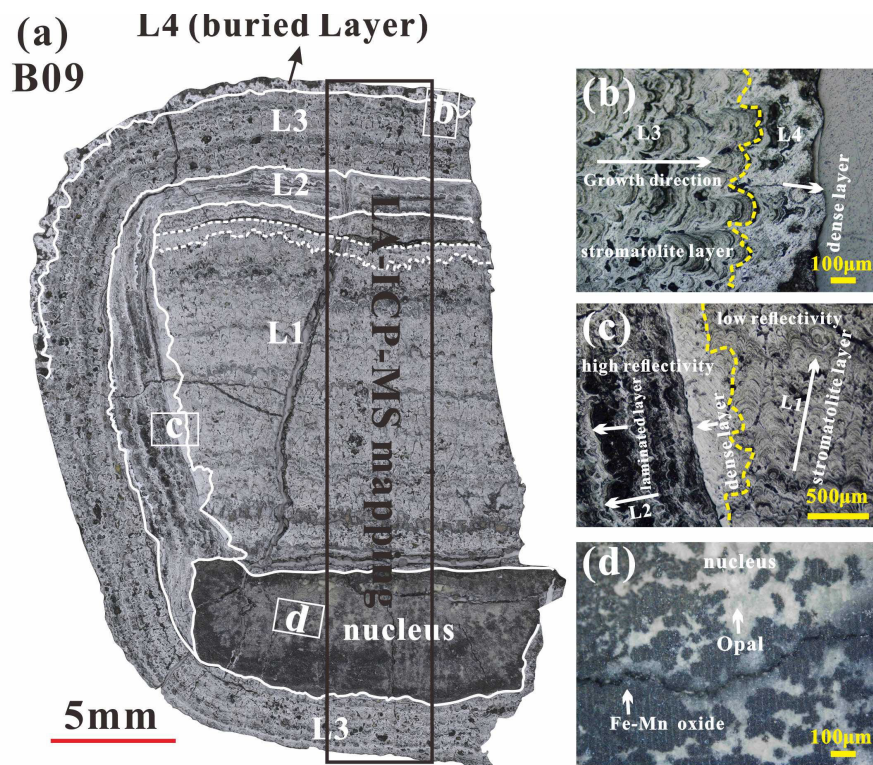
4.2. Geochemical Characteristics of the Ferromanganese Nodules

We define the genetic types of B09 and S12 based on two ternary genetic diagrams (Figure 3): $\text{Mn-Fe}-10 \times (\text{Ni} + \text{Cu})$ [21], $10 \times (\text{Cu} + \text{Ni} + \text{Co})-100 \times (\text{Zr} + \text{Y} + \text{Ce})-(\text{Fe} + \text{Mn})/4$ [22].

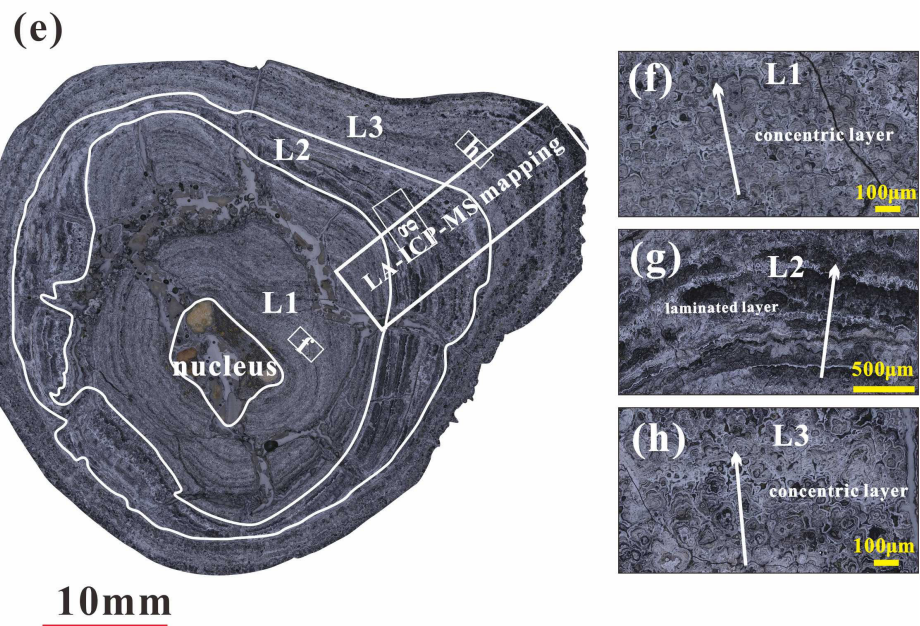
The results indicate that there is no significant difference in the geochemical characteristics between the L1, L2, and L3 of B09 and S12. Both L1 and L2 exhibit a mixed origin, but the data points are more inclined towards a hydrogenetic genesis type.

It is worth noting that the L4 of B09 data points is located in the oxic-suboxic diagenetic origin, and its element data distribution does not significantly coincide with B09-L2 and S12-L2 (Figure 3e,f), indicating that B09 received a higher proportion of diagenetic end element input.

The major and trace element content of B09 nodules are shown in Figure 4. There is significant element fractionation between the hydrogenetic and the diagenetic growth layer, with the hydrogenetic layer (L1, L3) being more enriched in Fe, Si, Ca, Ti, P, Sc, Zr, ΣREE , while the diagenetic layer (L2, L4) is enriched in Mn, Ba, Ni, Cu, Zn, Mg, Li, Mo, W, Al.



Shallow buried nodule



Surface nodule

Figure 2. Reflected light images of the B09 (a), and S12 (e). (b): Indicating the stromatolite structure of B09–L3 and the dense block like structure of B09–L4. (c): Indicating the laminated structure of B09–L2 and the stromatolite structure of B09–L1. There is a clear hiatus between the L2 and L1. (d): Indicating the opal core that has been replaced by ferromanganese oxides. (f): Indicating concentric circular structure of S12–L1, (g): Indicating laminated structure of S12–L2. (h): Indicating concentric circular structure of S12–L3. The solid lines represent the boundaries between different growth layers, and the white dashed lines indicate the boundaries of secondary growth layers.

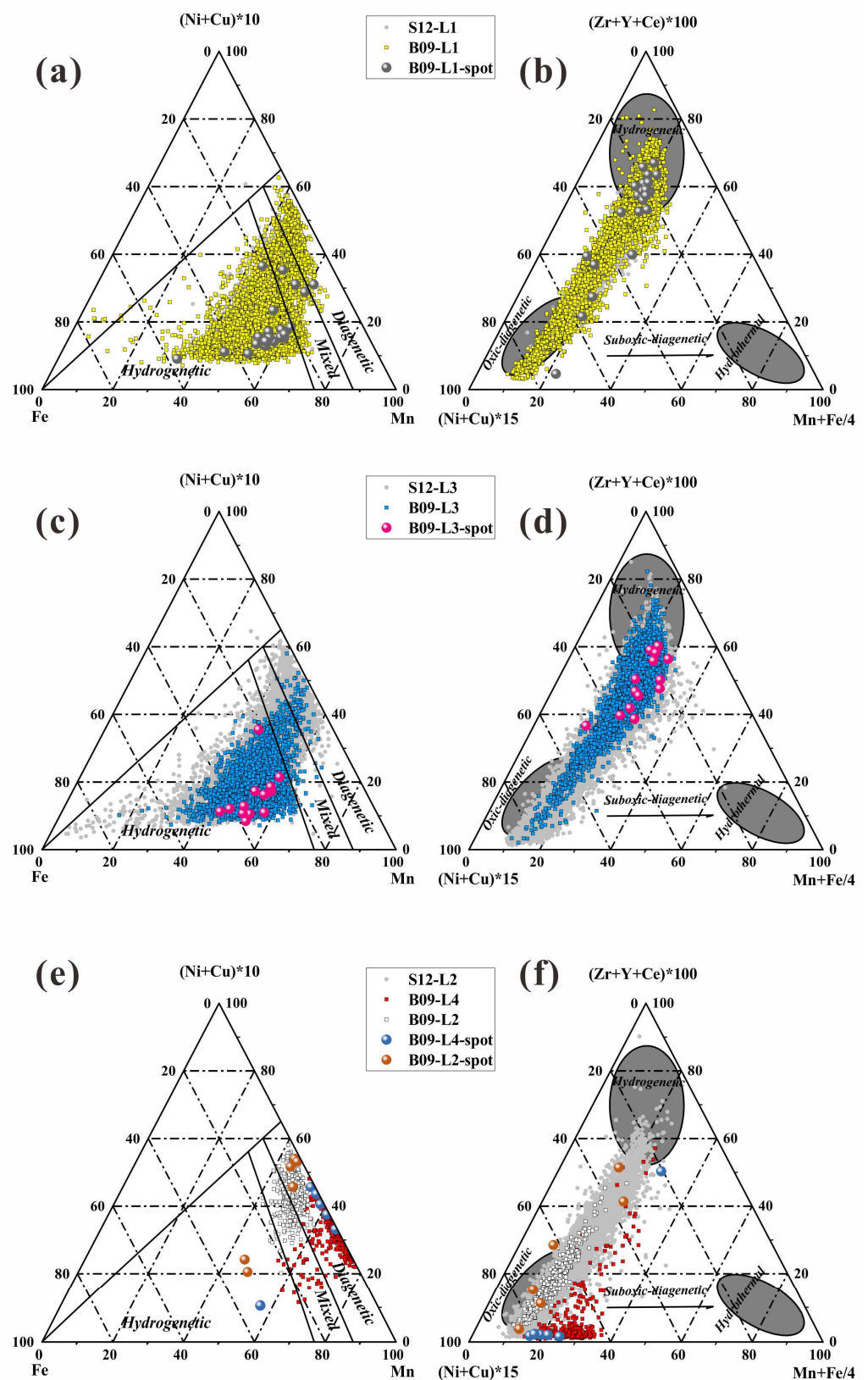


Figure 3. Ternary genetic diagram of Mn–Fe–(Ni + Cu)*10 [21] and (Mn + Fe)/4–(Cu + Ni)*15–(Zr + Y + Ce)*100 for ferromanganese nodules [22]. The basic data set is primarily composed of data extracted from LA-ICP-MS point analysis and surface scanning. (a,b) includes datasets of L1 layer in two nodules B09 and S12. (c,d) includes datasets of L3 layer in two nodules B09 and S12. (e,f) includes datasets of L2 and L4 layers in nodules B09 and S12.

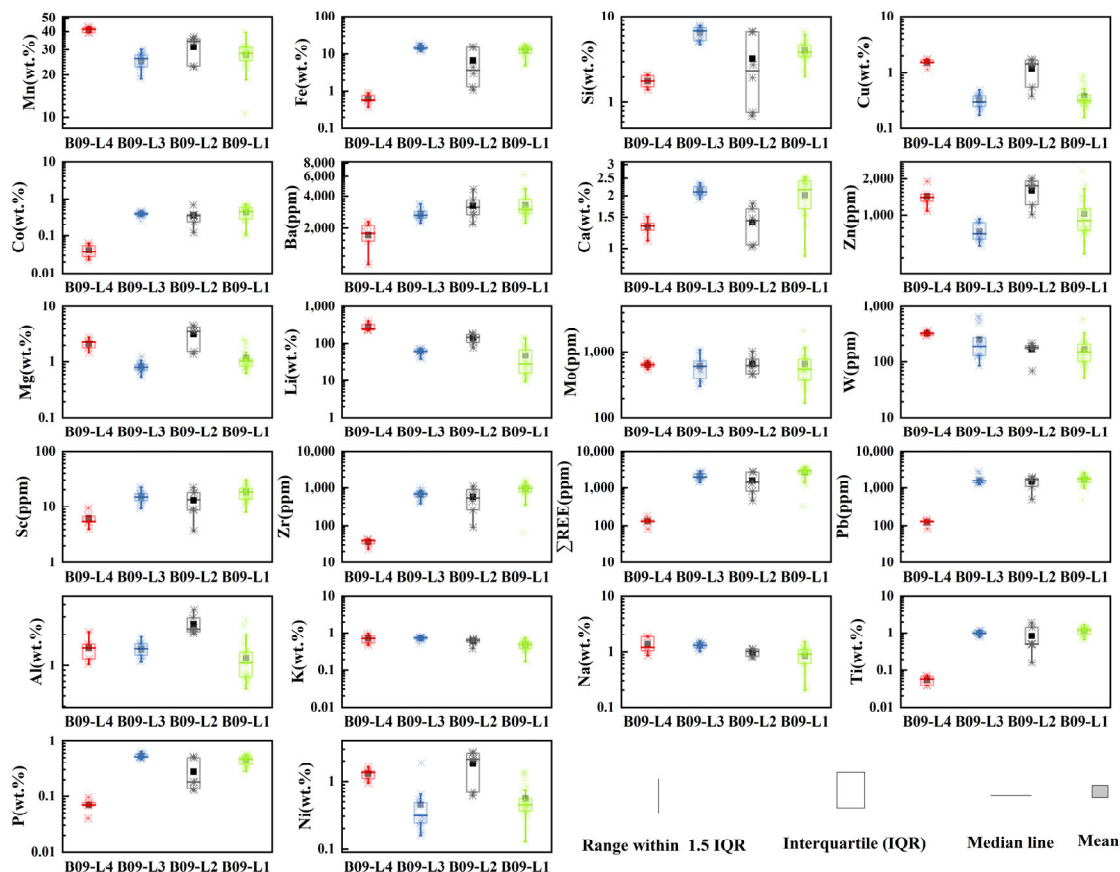


Figure 4. Comparative box plot of major and trace elements in B09.

It is worth noting that in comparison to the element content between the diagenetic layers (L2, L4), L4 exhibits higher average concentrations of Mn (41.2 vs. 31.2 wt%), W (328 vs. 170 ppm), and Li (290 vs. 140 ppm), but lower concentrations of hydroge-netic end member elements such as Fe (0.62 vs. 6.78 wt%), Co (0.04 vs. 0.35 wt%), REE (131 vs. 1600 ppm), Ti (0.05 vs. 0.84 wt%), Sc (6.23 vs. 13.13 ppm), Pb (124 vs. 1475 ppm) and diagenetic end member element such as Ni (1.29 wt% vs. 1.8 wt%) and Mg (2.13 vs. 3.16 wt%) in comparison to L2.

We use the empirical formula $R(\text{mm}/\text{Ma}) = 13.8 (\text{Mn}/\text{Fe}^2) + 0.75$ [23] to estimate the growth rate of the nodules. The results show that the average growth rate of L4 is 1977.6 mm/Ma, which is significantly higher than the diagenetic L2 (135.4 mm/Ma) and the hydrogenic L1 (4.47 mm/Ma) and L3 (2.4 mm/Ma).

4.3. Principal Components Analysis of B09

A PCA (principal components analysis) can visualize the complexity in a multidimensional dataset with information on the specific metal associations [24,25]. We assume that $\text{Mn}/\text{Fe} \approx 2.5$ is the boundary between the hydroge-netic and diagenetic layers (Halbach et al., 1981). PCA analysis was conducted on the elemental content of the four layers mentioned above (Figure 5), and the results showed that the elements in the nodules are mainly controlled by PC1 and PC2, with PC1 + PC2 accounting for 45.2%–59.9%.

There is a strong correlation between Mn, Ni, Cu, Mg, Li, W, Mo, and Zn, and the above elements are more affected by PC2. It is speculated that PC2 is a sedimentary pore water mineralization environment. Fe, Pb, Zr, Ti, Co, REE, and Sc are more controlled by PC1, suggesting that PC1 indicates the sedimentary environment of marine bottom water. The loadings of Na, Al, Si, and P in PC1 and PC2 are relatively small, while PC3 has a significant impact on these elements, which may be influenced by sedimentary debris.

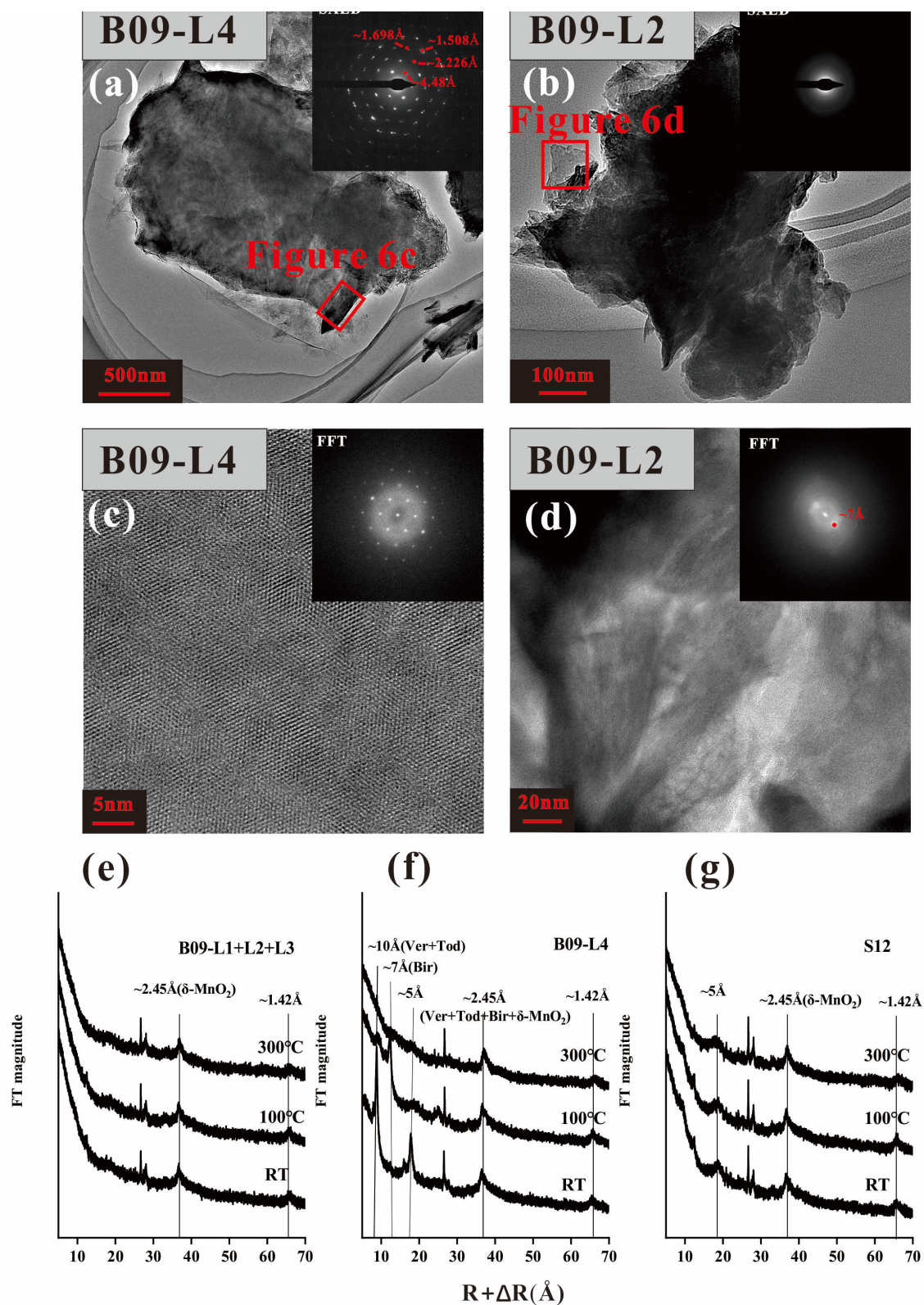


Figure 6. HRTEM images of L4 (a) and L2 (b) Mn minerals in B09 were inserted with the corresponding selected area electron diffraction (SAED) patterns. (c): Typical 120° twinning of todorokite (red square in (a)) corresponded with FFT (Fast Fourier transform) patterns. (d): HRTEM image and insert FFT pattern of L2 in a representing birnessite with fibrous parallel lattice fringes at 7 Å. (e): The XRD patterns of L1, L2 and L3 in B09. (f): The XRD patterns of L4 in B09. (g): The XRD patterns of a bulk sample of S12.

Todorokite has a stable tunnel-like structure and is not easily altered under vacuum or heating conditions [28–30]. However, its thermal stability may decrease due to irregular arrangements of the $[\text{MnO}_6]$ octahedron or the larger diameter of tunnel size [4,31,32]. The lower thermodynamic stability and lower crystallinity of todorokite in nodules may result in similar periodicity of todorokite and 10 Å vernadite in XRD spectra, making them difficult to distinguish. However, this cannot be taken as evidence of the non-existence of todorokite.

The mineral structure characteristics of the two diagenetic layers in nodule B09 are illustrated (Figure 6a–d). It is worth noting that the manganate in L4 exhibits a plate-like and fibrous morphology, as shown in Figure 6a. Selected area electron diffraction (SAED) analysis indicates that the mineral possesses well-defined crystallinity, with d-spacing values of hkl reflections matching those of todorokite (4.48 Å, 2.226 Å, 1.698 Å, and 1.508 Å) [33]. Fast Fourier transform (FFT) images (Figure 6c) reveal a triplet pattern of fiber crystals that are twinned at 120° angles from each other (Figure 6c). The 10 Å-manganate in L4 exhibited better crystallization (Figure 6c,d), possibly due to the higher influx of Mn^{2+} provided by the sediment pore water [6]. L2 layer reveals diffuse hk0 diffraction rings with d-spacing of 2.4 and 1.4 Å (Figure 6b), combined with $d = 7$ Å in FFT images (Figure 6d), could be indicative of 7 Å vernadite [32], which may result from the dehydration and condensation of 10 Å manganate [29].

5. Discussion

Due to the continuous uplift of the strata, the previously formed old nodule fragments are exposed on the surface of the sediment and enveloped by new growth shells, while buried nodules that have not been uplifted from the sediment surface are still left in the sediment [7,34]. However, in this study, the internal growth layers (L1, L2, L3) of surface nodule S12 and shallowly buried nodule B09 had similar structures and chemical compositions, while the L4, developed geochemical characteristics that were completely different (Figure 3f).

Therefore, we speculate that the shallow buried nodules might be a product of entering the burial stage after the formation of surface nodules and may continue to grow and develop the L4 growth layer after burial.

5.1. Controls on the Mineralogy of Buried Layer

The dominant mineral composition of diagenetic nodules is primarily 10 Å-vernadite, with a relatively low content of todorokite [29]. Todorokite is mainly found in buried nodules. As the burial depth of the nodules increases, the proportion of todorokite gradually increases [8,35]. In this study, the unique presence of todorokite in the L4 layer suggests that todorokite may be a characteristic mineral of buried-type nodules.

Mn^{3+} plays a critical role in facilitating the formation of todorokite in the reflux product [36,37]. The $[\text{Mn(III)O}_6]$ can act as pillars, providing support for the tunnel structure of todorokite [36,38]. In this study, under suboxic conditions, free Mn^{2+} in the sediment pore water would migrate upwards and react with MnO_2 above the oxic-suboxic boundary (OSF), resulting in the generation of Mn^{3+} [35]. The suboxic conditions prevalent in the sediment maintain a considerable concentration of Mn^{3+} [39,40]. This abundance of Mn^{3+} allows it to enter the 10 Å-vernadite and promote the formation of the tunnel walls of todorokite [32,36]. It is worth noting that the elongation of Mn(III)-O along the a-axis may facilitate folding at the Mn(III)-O-Mn(IV) junctions due to the Jahn-Teller effect [27,31]. In summary, we suggest that todorokite could potentially serve as an indicator mineral for manganese nodules undergoing burial processes.

5.2. Controls on the Geochemistry of L4 in Buried Nodules

5.2.1. Controls on the Chemical Composition of L4

The L1 and L3 datasets of B09 and S12 nodules consistently fell within the hydrogenetic and oxic-diagenetic layers on the ternary genetic diagram (Figure 3a–d). However, L4

datasets fell within the range of oxic-diagenetic to suboxic-diagenetic, suggesting that its mineral source could primarily originate from sediment pore water.

The content of hydrogenetic end member elements in L4 is significantly lower than that in L2 (Figure 4). This may be due to the fact that L2 starts growing on the surface of sediments, developing δ -MnO₂ and receiving detrital supply from deep-sea bottom water. The Fe-Mn oxyhydroxides in L2 have a larger reactive surface area [1], enabling efficient adsorption of high-field strength elements (HFSE) such as Sc, Zr, rare earth elements (REEs), and Pb [22].

The dissolution of organic matter in sediments releases a significant amount of transition metals, leading to higher fluxes of diagenetic elements entering the nodules [1,6]. However, it is worth noting that the content of diagenetic elements in the L4 is lower compared to the L2. We suggest that there may be two possible reasons for this phenomenon.

Phyllosulfate minerals usually have low-valence isomorphous ions replacing Mn⁴⁺, resulting in layer charge defects which can be compensated for by incorporating hydrated interlayer ions like Na⁺, Li⁺, and Ca²⁺ into the interlayer space, or by adsorbing cations such as Mn²⁺, Ni²⁺, Cu²⁺, Zn²⁺, and Cr²⁺ in vacant sites below the MnO₆ octahedral layers [27,41,42]. Todorokite, on the other hand, has limited tunnel structures that can adsorb monovalent and divalent cations [32]. Therefore, the L2 layer, rich in phyllosulfate minerals, has a higher potential than L4 to attract metal cations [27,32,33].

On the other hand, during the growth process of L4, the increase in Mn flux in the sediment [6] leads to competition between Mn²⁺ and other metals, such as Ni²⁺, Cu²⁺, Co²⁺, Ca²⁺, Mg²⁺, to preferentially incorporate into the manganese mineral crystal [6,11].

5.2.2. The Formation of B09-L4

The process of oxic diagenesis is believed to take place within nodules embedded in oxygenated sediments through a sequence of sedimentary processes and chemical reactions [43]. This process is characterized by moderate Mn/Fe ratios and high Ni and Cu concentrations [11,44]. In the current study, the L4 is identified within sub-surface sediments at a depth of 60 cm. Given that the OSF is approximately 2–3 m deep in the eastern part of the CCFZ [9], and considering the lower surface productivity in the western part of the CCFZ compared to the east [15,45] and Antarctic Bottom Water (AABW) flows from west to east in the CCFZ [46], it is anticipated that the OSF depth in the western part should exceed 2 m. Consequently, the growth position of L4 is expected to be above the OSF, indicating an association with oxic diagenetic processes. However, the B09 nodule displays higher Mn/Fe ratios and lower Ni and Cu concentrations (Figure 4), which do not correspond with the oxic diagenesis interval illustrated in the ternary plot.

The growth rate of L4 is about 1977.6 mm/Ma, significantly higher than the growth rate of L2 (135.4 mm/Ma). However, the thickness of the L4 layer is only 0.3 mm, indicating that the growth of the L4 layer may be transient.

Our investigation in the area revealed that the surrounding sediment where buried nodules are located mainly consists of compacted pelagic clay, with limited pore water flow. This suggests that the conditions necessary for sustained growth of the L4 layer may not be met.

Therefore, the formation of the L4 could be attributed to large seasonal variations in primary productivity on the surface [43,47]. This leads to a temporary surge in oxygen consumption in surface sediments and the development of a transient suboxic environment [48] above the OSF. In this suboxic environment, manganese oxides in surface sediments dissolve, releasing Mn²⁺ and associated elements trapped in organic matter particles [9]. This process may directly contribute to the growth of the oxic-suboxic diagenetic layer.

5.2.3. Multiple Sources Control the Growth of Nodules

The substantial overlap between the datasets of the inner layers (L1, L2, L3) of B09 and S12 nodules suggests that there was a limited exchange of Ni, Cu, and Co with the pore water of the sediment during the burial process of B09 (Figure 7).

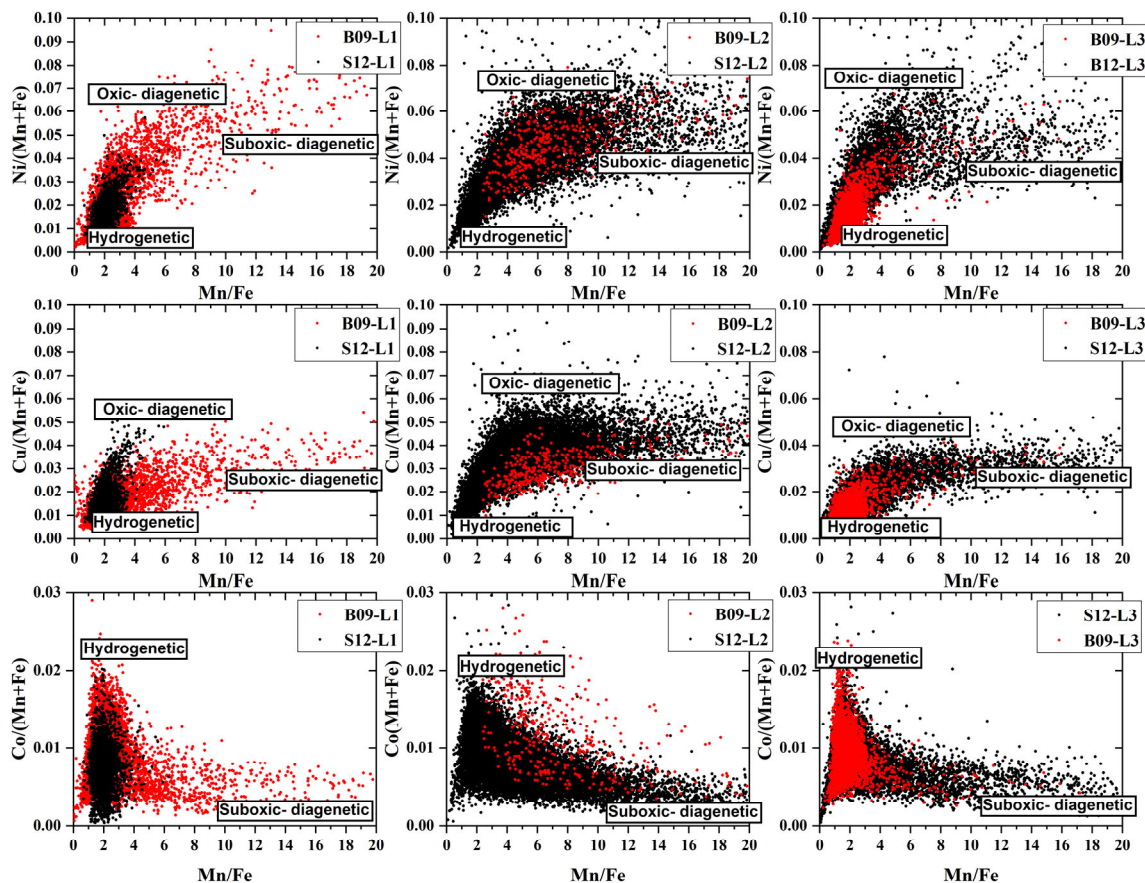


Figure 7. Relationships of Mn/Fe with Ni/(Mn + Fe), Cu/(Mn + Fe), and Co/(Mn + Fe) in S12 and B09 (red points represent the buried nodule B09 and black points represent the surface nodule S12).

The correlation diagrams between Ni, Cu, Co, and Mn/Fe in S12 and B09 were generated using the LA-ICP-MS element dataset. These diagrams provide valuable insights by overcoming the limitations of data volume in in-situ microanalysis (Figure 7) [49]. The distribution of each element is influenced by three end members, indicating three genetic processes: low Mn/Fe ($Mn/Fe < 2$) with low Ni/(Mn + Fe) and Cu/(Mn + Fe) (0–0.02), as well as high Co/(Mn + Fe) (0.02), indicating hydrogenetic, medium Mn/Fe ($Mn/Fe \approx 5$) with high Ni/(Mn + Fe) (0.07), Cu/(Mn + Fe) (0.06) indicating oxidic-diagenesis, and high Mn/Fe with low Ni/(Mn + Fe) (0.04), Cu/(Mn + Fe) (0.03), and Co/(Mn + Fe) (0.02) indicating suboxic diagenesis [50]. However, the data combination points are mainly concentrated on one side of the hydrogenetic endmember, which may indicate that hydrogenetic deposition remains the primary sedimentary process for nodules. The instantaneous change in surface primary productivity could lead to changes in the sedimentary environment and may provide sources for nodules of oxidic diagenetic and suboxic diagenetic (Section 5.2.2)

It is worth noting that in the individual layers of nodules, Co shows a sudden change in element content at $Mn/Fe \approx 2$, while Ni and Cu show a change in element content around $Mn/Fe \approx 5$. This may be due to changes in mineral composition during the sediment environment transformation from oxidic diagenetic to sub-oxic diagenetic [6,51].

5.3. Mineralization Pattern of Shallow Buried Nodule

Based on the mineralogical and element distribution characteristics observed in this study, we have developed a mineralization model to explain the growth process of shallow buried nodules in the western part of the CCFZ (Figure 8). The L1 layer is characterized by the growth of concretions around opal. Low surface primary productivity and the deep depth of OSF favor the formation of a hydrogenetic growth layer. As the surface primary productivity increases, the nodules may undergo burial and dissolution of the L1

layer [8]. When the sedimentation rate decreases and sedimentation becomes intermittent, the nodules re-emerge on the sediment surface and develop the L2 growth layer, receiving a pore water supply from the sediment. As the nodules continue to uplift [7], they receive water and material supply from the bottom deep-sea water [1], leading to the development of the L3 growth layer.

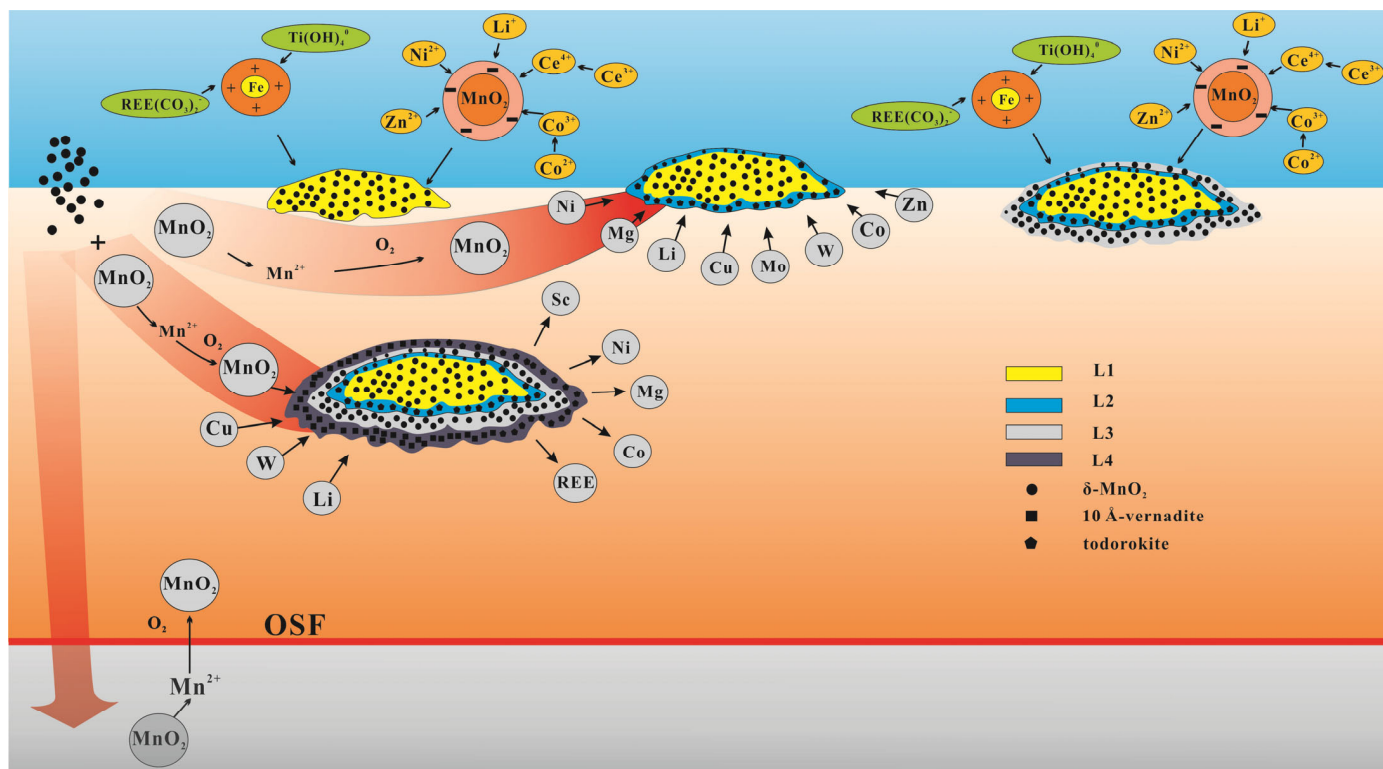


Figure 8. Schematic diagram of shallow buried nodule and surface nodule growth model in the western part of CCFZ. The surface nodules develop a three-layer structure, with their original development positions located on the surface of the sediment. Shallow buried nodules are products of the continued growth of surface nodules after being buried. The relatively sub-oxidized sedimentary environment causes the formation of todorokite in the outer layer of shallow buried nodules. The high Mn flux and differences in mineral composition result in relatively poor elements such as Ni, Mg, Co, Ca, etc. in shallowly buried nodules.

After that, local increases in sedimentation rate or tectonic activity may have influenced some nodules to be buried within the sediments. Influenced by large seasonal variations in primary productivity, the increase in organic carbon flux at the seafloor could lead to an increase in oxygen consumption, which could further result in the significant reduction of MnO_2 , buried nodules continue to grow above the OSF.

Note that this study is only based on the analysis of two nodules (B09 and S12). Important scientific conclusions and the geochemical model of the pore water-sediment-nodules reaction must be confirmed on a larger population of samples.

6. Conclusions

This study aims to clarify the mineral composition, elemental geochemical behavior, and formation processes of buried polymetallic nodules in the western part of CCFZ. The buried nodules were further classified into three growth layers: L1 (hydrogenetic), L2 (oxic diagenetic), and L3 (hydrogenetic). Additionally, a new oxic-suboxic diagenetic type, L4, was identified, emerging from L3.

L4 shows higher contents of Mn, Li, and W, while the contents of Fe, Co, REE, Sc, Pb, Ti, Ni, and Mg are relatively lower. We suggest that L4 could not be affected by the bottom

water source. The presence of todorokite and the high flux of Mn^{2+} in the sediment pore water compete with other metal elements to enter the lattice of manganate, thereby leading to a significant difference in elemental content between the two diagenetic layers.

An instantaneous increase in surface primary productivity could result in a temporary rise in oxygenated sediment flux (OSF), enabling the upward movement of Mn^{2+} to support the growth of L4. The instantaneous changes in the sedimentary environment may ultimately result in alternating deposition of hydrogenetic, oxic diagenetic, and suboxic diagenetic processes within the nodules.

Author Contributions: Conceptualization, Y.D. and Z.F.; methodology, X.L. and W.M.; software, Z.L.; validation, H.W., J.L. and Z.Z.; formal analysis, Z.F.; investigation, Z.F.; resources, X.L. and H.L.; data curation, K.Y.; writing—original draft preparation, Z.F.; writing—review and editing, Y.D.; visualization, Y.D.; supervision, X.L.; project administration, F.C.; funding acquisition, X.L. All authors have read and agreed to the published version of the manuscript.

Funding: This research was financially supported by the National Natural Science Foundation of China (U2244222), the National Key R&D Program of China (Grant No.2023YFC2811305 and 2022YFC2806601), the Resources and Environment Projects of China Ocean Mineral R&D Association (DY135-G2-1, DY135-N2-1).

Data Availability Statement: Datasets related to this article can be found at <http://dx.doi.org/10.17632/6jsts84xn5.1>, an open-source online data repository hosted at Mendeley Data.

Acknowledgments: We sincerely thank the scientists and crew of the voyages DY73 for providing precious samples.

Conflicts of Interest: The authors declare no conflicts of interest.

References

1. Hein, J.R.; Koschinsky, A.; Kuhn, T. Deep-ocean polymetallic nodules as a resource for critical materials. *Nat. Rev. Earth Environ.* **2020**, *1*, 158–169. [[CrossRef](#)]
2. Koschinsky, A.; Hein, J.R. Uptake of elements from seawater by ferromanganese crusts: Solid-phase associations and seawater speciation. *Mar. Geol.* **2003**, *198*, 331–351. [[CrossRef](#)]
3. Halbach, P.; Giovanoli, R.; Borstel, D.V. Geochemical processes controlling the relationship between Co, Mn, and Fe in early diagenetic deep-sea nodules. *Earth Planet. Sci. Lett.* **1982**, *60*, 226–236. [[CrossRef](#)]
4. Burns, R.G.; Burns, V.; Harlan, W.S. A review of the todorokite-buserite problem: Implications to the mineralogy of marine manganenodules. *Am. Mineral.* **1983**, *68*, 972–980. [[CrossRef](#)]
5. Hein, J.R.; Mizell, K.; Koschinsky, A.; Conrad, T.A. Deep-ocean mineral deposits as a source of critical metals for high- and green-technology applications: Comparison with land-based resources. *Ore Geol. Rev.* **2013**, *51*, 1–14. [[CrossRef](#)]
6. Halbach, P.; Scherhag, C.; Heibisch, U.; Marchig, V. Geochemical and mineralogical control of different genetic types of deep-sea nodules from the Pacific Ocean. *Miner. Depos.* **1981**, *16*, 59–84. [[CrossRef](#)]
7. Usui, A.; Nishimura, A.; Mita, N. Composition and growth history of surficial and buried manganese nodules in the Penrhyn Basin, Southwestern Pacific. *Mar. Geol.* **1993**, *114*, 133–153. [[CrossRef](#)]
8. Heller, C.; Kuhn, T.; Versteegh, G.J.M.; Wegorzewski, A.V.; Kasten, S. The geochemical behavior of metals during early diagenetic alteration of buried manganese nodules. *Deep. Sea Res. Part. Oceanogr. Res. Pap.* **2018**, *142*, 16–33. [[CrossRef](#)]
9. Mewes, K.; Mogollón, J.M.; Picard, A.; Rühlemann, C.; Kuhn, T.; Nöthen, K. Impact of depositional and biogeochemical processes on small scale variations in nodule abundance in the Clarion-Clipperton Fracture Zone. *Deep. Sea Res. Part. Oceanogr. Res. Pap.* **2014**, *91*, 125–141. [[CrossRef](#)]
10. Halbach, P.; Friedrich, G.; Stackelberg, U.V. *The Manganese Nodule Belt of the Pacific Ocean: Geological Environment, Nodule Formation, and Mining Aspects*; F. Enke: Barcelona, Spain, 1988.
11. Wegorzewski, A.V.; Kuhn, T. The influence of suboxic diagenesis on the formation of manganese nodules in the Clarion Clipperton nodule belt of the Pacific Ocean. *Mar. Geol.* **2014**, *357*, 123–138. [[CrossRef](#)]
12. Chester, R.; Jickells, T. *Nutrients, Oxygen, Organic Carbon and the Carbon Cycle in Seawater*; John Wiley Sons Ltd.: Hoboken, NJ, USA, 2012; pp. 163–207. [[CrossRef](#)]
13. Mcallister, C.D.; Parsons, T.R.; Strickland, J.D.H. Primary Productivity and Fertility at Station “P” in the North-East Pacific Ocean. *ICES J. Mar. Sci.* **1960**, *25*, 240–259. [[CrossRef](#)]
14. Pau, F.; Cara, W. Phytoplankton productivity in the North Pacific ocean since 1900 and implications for absorption of anthropogenic CO_2 . *Nature* **1992**, *358*, 741–743. [[CrossRef](#)]
15. Glasby, G.P. *Manganese: Predominant Role of Nodules and Crusts*; Springer: Berlin/Heidelberg, Germany, 2006. [[CrossRef](#)]

16. Li, D.; Fu, Y.; Liu, Q.; Reinfeld, J.R.; Hollings, P.; Sun, X. High-resolution LA-ICP-MS mapping of deep-sea polymetallic micronodules and its implications on element mobility. *Gondwana Res.* **2020**, *81*, 461–474. [[CrossRef](#)]
17. Xu, H.; Shen, Z.; Konishi, H. Natural occurrence of monoclinic Fe₃S₄ nano-precipitates in pyrrhotite from the Sudbury ore deposit: A Z-contrast imaging and density functional theory study. *Mineral. Mag.* **2015**, *79*, 377–386. [[CrossRef](#)]
18. Jochum, K.P.; Weis, U.; Stoll, B.; Kuzmin, D.; Enzweiler, J. Determination of Reference Values for NIST SRM 610–617 Glasses Following ISO Guidelines. *Geostand. Geoanalytical Res.* **2015**, *35*, 397–429. [[CrossRef](#)]
19. Liu, Y.; Hu, Z.; Gao, S.; Detlef, G.; Xu, J. In situ analysis of major and trace elements of anhydrous minerals by LA-ICP-MS without applying an internal standard. *Chem. Geol.* **2008**, *257*, 34–43. [[CrossRef](#)]
20. Chen, L.; Liu, Y.; Hu, Z.; Gao, S.; Zong, K.; Chen, H. Accurate determinations of fifty-four major and trace elements in carbonate by LA-ICP-MS using normalization strategy of bulk components as 100%. *Chem. Geol.* **2011**, *284*, 283–295. [[CrossRef](#)]
21. Bonatti, E.; Kraemer, T.; Rydell, H. Classification and genesis of submarine iron-manganese deposits. *Ferromanganese Depos Ocean Floor* **1972**, *19*, 149–166.
22. Josso, P.; Pelletier, E.; Pourret, O.; Fouquet, Y.; Etoubleau, J.; Cheron, S. A new discrimination scheme for oceanic ferromanganese deposits using high field strength and rare earth elements. *Ore Geol. Rev.* **2017**, *87*, 3–15. [[CrossRef](#)]
23. Teh-Lung, C.A. Radiochemical observations on manganese nodules from three sedimentary environments in the north Pacific. *Geochim. Cosmochim. Acta* **1984**, *48*, 951–963. [[CrossRef](#)]
24. Oyebamiji, A.; Hu, R.; Zhao, C.; Zafar, T. Origin of the Triassic Qilinchang Pb-Zn deposit in the western Yangtze block, SW China: Insights from in-situ trace elemental compositions of base metal sulphides. *J. Asian Earth Sci.* **2020**, *192*, 104292. [[CrossRef](#)]
25. Toffolo, L.; Nimis, P.; Gennady, A.T.; Melekestseva, I.Y.; Beltenev, V.E. Seafloor massive sulfides from mid-ocean ridges: Exploring the causes of their geochemical variability with multivariate analysis. *Earth-Sci. Rev. Int.* **2020**, *201*, 102958. [[CrossRef](#)]
26. Chukhrov, F.V.; Drits, V.A.; Gorshkov, A.I. Structural transformations of manganese oxides in oceanic nodules. *Int. Geol. Rev.* **1987**, *29*, 110–121. [[CrossRef](#)]
27. Manceau, A.; Lanson, M.; Takahashi, Y. Mineralogy and crystal chemistry of Mn, Fe, Co, Ni, and Cu in a deep-sea Pacific polymetallic nodule. *Am. Mineral.* **2014**, *99*, 2068–2083. [[CrossRef](#)]
28. Shen, Y.F.; Zenger, R.P. Manganese oxide octahedral molecular sieves: Preparation, characterization, and applications. *Science* **1993**, *260*, 511–515. [[CrossRef](#)] [[PubMed](#)]
29. Wegorzewski, A.V.; Kuhn, T.; Dohrmann, R.; Wirth, R.; Grangeon, S. Mineralogical characterization of individual growth structures of Mn-nodules with different Ni+Cu content from the central Pacific Ocean. *Am. Mineral.* **2015**, *100*, 2497–2508. [[CrossRef](#)]
30. Post, J.E.; Veblen, D.R. Crystal structure determinations of synthetic sodium, magnesium, and potassium birnessite using TEM and the Rietveld method. *Am. Mineral.* **1990**, *75*, 477–489. [[CrossRef](#)]
31. Usui, A.; Mellin, T.A.; Nohara, M.; Yuasa, M. Structural stability of marine 10 Å manganates from the Ogasawara (Bonin) Arc: Implication for low-temperature hydrothermal activity. *Mar. Geol.* **1989**, *86*, 41–56. [[CrossRef](#)]
32. Bodeř, S.; Manceau, A.; Geoffroy, N.; Baronnet, A.; Buatier, M. Formation of todorokite from vernadite in Ni-rich hemipelagic sediments. *Geochim. Cosmochim. Acta* **2007**, *71*, 5698–5716. [[CrossRef](#)]
33. Atkins, A.L.; Shaw, S.; Peacock, C.L. Release of Ni from birnessite during transformation of birnessite to todorokite: Implications for Ni cycling in marine sediments. *Geochim. Cosmochim. Acta* **2016**, *189*, 158–183. [[CrossRef](#)]
34. Stackelberg, U.V. Significance of benthic organisms for the growth and movement of manganese nodules, Equatorial North Pacific. *Geo-Mar. Lett.* **1984**, *4*, 37–42. [[CrossRef](#)]
35. Wegorzewski, A.V.; Grangeon, S.; Webb, S.M.; Heller, C.; Kuhn, T. Mineralogical transformations in polymetallic nodules and the change of Ni, Cu and Co crystal-chemistry upon burial in sediments. *Geochim. Cosmochim. Acta* **2020**, *282*, 19–37. [[CrossRef](#)]
36. Grangeon, S.; Lanson, B.; Lanson, M. Solid-state transformation of nanocrystalline phyllo-manganate into tectomanganate: Influence of initial layer and interlayer structure. *Acta Crystallogr.* **2014**, *70*, 828–838. [[CrossRef](#)] [[PubMed](#)]
37. Wu, Z.; Lanson, B.; Feng, X.; Yin, H.; Liu, F. Transformation of Ni-containing birnessite to tectomanganate: Influence and fate of weakly bound Ni(II) species. *Geochim. Cosmochim. Acta* **2019**, *271*, 96–115. [[CrossRef](#)]
38. Grangeon, S.; Fernandez-Martinez, A.; Warmont, F.; Gloter, A.; Marty, N.; Poulain, A.; Lanson, B. Cryptomelane formation from nanocrystalline vernadite precursor: A high energy X-ray scattering and transmission electron microscopy perspective on reaction mechanisms. *Geochem. Trans.* **2015**, *16*, 12. [[CrossRef](#)] [[PubMed](#)]
39. Elzinga, E.J. ⁵⁴Mn Radiotracers Demonstrate Continuous Dissolution and Re-precipitation of Vernadite (δ-MnO₂) during Interaction with Aqueous Mn(II). *Environ. Sci. Technol.* **2016**, *50*, 8670–8677. [[CrossRef](#)] [[PubMed](#)]
40. Grangeon, S.; Warmont, F.; Tournassat, C.; Lanson, B.; Lanson, M.; Elkam, E. Nucleation and growth of feitknechtite from nanocrystalline vernadite precursor. *Eur. J. Mineral.* **2017**, *29*, 767–776. [[CrossRef](#)]
41. Manceau, A.; Kersten, M.; Marcus, M.A.; Geoffroy, N.; Granina, L. Ba and Ni speciation in a nodule of binary Mn oxide phase composition from Lake Baikal. *Geochim. Cosmochim. Acta* **2007**, *71*, 1967–1981. [[CrossRef](#)]
42. Peacock, C.L.; Sherman, D.M. Crystal-chemistry of Ni in marine ferromanganese crusts and nodules. *Am. Mineral.* **2007**, *92*, 1087–1092. [[CrossRef](#)]
43. Dymond, J.; Lyle, M.; Rnney, B.; Piper, D.Z. Ferromanganese nodules from MANOP Sites H, S, and R—Control of mineralogical and chemical composition by multiple accretionary processes. *Geochim. Cosmochim. Acta* **1984**, *48*, 931–949. [[CrossRef](#)]

44. Blöthe, M.; Wegorzewski, A.; Müller, C.; Simon, F.; Kuhn, T.; Schippers, A. Manganese-Cycling Microbial Communities Inside Deep-Sea Manganese Nodules. *Environ. Sci. Technol.* **2015**, *49*, 7692–7700. [[CrossRef](#)] [[PubMed](#)]
45. Menendez, A.; James, R.H.; Lichtschlag, A.; Connelly, D.; Peel, K. Controls on the chemical composition of ferromanganese nodules in the Clarion-Clipperton Fracture Zone, eastern equatorial Pacific. *Mar. Geol.* **2019**, *409*, 1–14. [[CrossRef](#)]
46. Amos, A.F.; Roels, O.A. Environment aspects of manganese nodule mining. *Mar. Policy* **1977**, *1*, 156–163. [[CrossRef](#)]
47. Honjo, S. Seasonality and Interaction of Biogenic and Lithogenic Particulate Flux at the Panama Basin. *Science* **1982**, *218*, 883–884. [[CrossRef](#)]
48. Emerson, S.; Jahnke, R.; Bender, M. Early diagenesis in sediments from the eastern equatorial Pacific, I. Pore water nutrient and carbonate results. *Earth Planet. Sci. Lett.* **1980**, *49*, 57–80. [[CrossRef](#)]
49. Gourcerol, B.; Kontak, D.J.; Thurston, P.C.; Petrus, J.A. Application of La-Icp-MS Sulfide Analysis and Methodology for Deciphering Elemental Paragenesis and Associations in Addition to Multi-Stage Processes in Metamorphic Gold Settings. *Can. Mineral.* **2018**, *56*, 39–64. [[CrossRef](#)]
50. Su, R.; Sun, F.; Li, X.; Chu, F.; Sun, G.; Li, J.; Wang, H.; Li, Z.; Zhang, C.; Zhang, W.; et al. Diverse early diagenetic processes of ferromanganese nodules from the eastern Pacific Ocean: Evidence from mineralogy and in-situ geochemistry. *Int. Geol. Rev.* **2023**, *65*, 2131–2147. [[CrossRef](#)]
51. Cheng, Y. Chronology and critical metals enrichment mechanism of ferromanganese nodules from the Parece Vela Basin, Philippine Sea. *Chem. Geol.* **2023**, *630*, 121494. [[CrossRef](#)]

Disclaimer/Publisher’s Note: The statements, opinions and data contained in all publications are solely those of the individual author(s) and contributor(s) and not of MDPI and/or the editor(s). MDPI and/or the editor(s) disclaim responsibility for any injury to people or property resulting from any ideas, methods, instructions or products referred to in the content.